N-Ras forms dimers at POPC membranes

Jörn Güldenhaupt[1*], Till Rudack[1*], Peter Bachler[1], Daniel Mann[1], Gemma Triola[2], Herbert Waldmann[2], Carsten Kötting[1], and Klaus Gerwert[1]

[1] *Lehrstuhl für Biophysik, Ruhr-Universität Bochum, D-44780 Bochum*

[2] *Max Planck Institute of Molecular Physiology Dortmund, D-44227 Dortmund*

* *both authors contributed equally*

Supporting Material

Simulation parameters

MM simulations were performed with GROMACS 4.0.7 (1, 2) and the optimized potentials for liquid simulations all atom (OPLS/AA) force field (3), with guanosine-5'-triphosphate (GTP) and guanosine-5'-diphosphate (GDP) parameters, which have been improved regarding the reproduction of the dihedral energy surface. The TIP4P water model (4) and a POPC bilayer with the parameters of Ulmschneider et al. (5) were used. The farnesyl and palmitoyl anchors were parameterized by adopting parameters from comparable groups of the POPC membrane. During MM simulations, the electronic interactions of the system were evaluated using the Fast Particle-Mesh Ewald method (6) with a grid spacing of 0.12 nm and fourth-order spline interpolation. The van der Waals interactions between atom pairs were truncated within a cut-off value of 1.4 nm. A Berendsen thermostat with a coupling constant of 0.1 ps and a Berendsen barostat with a coupling constant of 1.0 ps were used to keep the system at a constant temperature and pressure of 310 K and 1 standard atmosphere, respectively (7). For the simulation system, a triclinic box was used with periodic boundary conditions. The simulations were run with an integration step of 2 fs and therefore, all bonds were constrained to their equilibrium distance by the LINCS algorithm (8). Quantum mechanics (QM) simulations were performed with Gaussian03 (9), and QM/MM simulations with the GROMACS/Gaussian interface (10) and the normal QM/MM scheme (11). All QM simulations were carried out with the B3LYP functional (12, 13) combined with the 6-31G* basis set.

Simulation systems

A homology model for N-Ras with the template X-ray structure of H-Ras·GDP (4Q21 AA 1-168 resolved was built using the SCRWL algorithm (14). N-Ras and H-Ras are 93% homologous with 86% identity. The main differences are in the hypervariable region (HVR) and the anchor region, neither of which have been resolved by X-ray or NMR analysis. The homology for the G domain alone is even higher with 97% identity. Therefore, the homology model for the G domain is very reliable. There is one X-Ray structure of the N-Ras G-domain (3CON) (15) available, but in this structure α-helix 2 is not resolved. The resolved parts of the X-ray structure are very similar compared to our homology model. The remaining regions of full-length N-Ras were modeled based on other experimental hints, as follows.

Comparison of the secondary structure analysis of the alpha-helical region of simulated full length N-Ras and H-Ras with the results from FTIR spectroscopic measurements (16) have shown that the helix 5 has to be extended from amino acid 168 to 172. Now, α-helix 5 ends at Ser173, which is followed by another serine. This is a typical motive for a helix ending. The dihedrals of the anchor region 180–186 are known from NMR studies (17), and indicate a horseshoe conformation for this region. The structure of the HVR, which has not yet been experimentally solved, was modelled using an all-trans conformation of the amino acid backbone.

The full-length N-Ras·GTP and N-Ras·GDP structures were then protonated, checked, and amended using the MAXIMOBY algorithm (18). These prepared structures were placed into a triclinic simulation box, filled with TIP4P water, and a POPC bilayer. To mimic the physiological salt concentration of 154 mmol/l, sodium cations and chlorine anions were added.

The quantum yield Q_0

Hiratsuka (1983) determined the quantum yield of Mant-GTP in water to be 0.24 (19). We expected the same quantum yield for Mant-GDP in water. To investigate the influence of binding of Mant-GDP to Ras on the quantum yield, we compared the static fluorescence emission spectra of Ras-bound and free Mant-GDP.

For this, Mant-GDP was bound to Ras via the EDTA method (20), followed by a 1-min gel filtration step (Zeba Spin Desalting Columns, Pierce Biotechnology, Rockford, IL, USA) in

which the buffer was exchanged to buffer E supplemented with 5 mM $MgCl_2$. Static fluorescence measurements were performed using a Jasco Spectrofluorometer FP 6500 (Gross-Umstadt, Germany). Ras·Mant-GDP (1 µM) in buffer E supplemented with 5 mM $MgCl_2$ was excited at 355 nm, and emission was detected from 390 to 600 nm. Mant-GDP was released from Ras by the addition of 10 mM EDTA and 100 µM non-fluorescent GDP. Emission spectra were successively recorded, reference-corrected, and integrated.

To compensate for bleaching, the solution was constantly stirred in a quartz cuvette. The overall emission (F) before the release of Mant-GDP from Ras (first spectrum) was compared to that after almost complete exchange (last spectrum) (Fig. S5), yielding Eq. S1

$$\Delta F = \frac{F_{bound}}{F_{unbound}} \approx \frac{29320}{19387} = 2.19\,. \qquad \textbf{(S1)}$$

This is why the assumed quantum yield of Mant-GDP (0.24 in solution, (19)) was adapted to be 0.24 · 2.19 = 0.53 when bound to Ras; this is established for the experiments presented here. Similar changes of Q_0 have been observed for Mant-labeled guanosine nucleotides due to binding to Ras (21).

Determination of the overlap integral J between Mant and TNP

The overlap integral, which represents the spectral overlap between the donor fluorescence and the acceptor absorbance in units [$nm^4\ M^{-1}\ cm^{-1}$], is another important parameter for the calculation of R_0 and is derived from Eq. S2:

$$J(\lambda) = \frac{\int_{-\infty}^{\infty} F_D(\lambda) \cdot \varepsilon_A(\lambda) \cdot \lambda^4\, d\lambda}{\int_{-\infty}^{\infty} F_D(\lambda)\, d\lambda} \qquad \textbf{(S2)}$$

Here, $F_D(\lambda)$ and $\varepsilon_A(\lambda)$ are the donor emission and the extinction coefficient of the acceptor at a given wavelength λ, respectively. Absorbance spectra of 10 µM TNP-GDP in buffer E supplemented with 5 mM $MgCl_2$ were recorded between 370 and 650 nm in steps of 2 nm using an Uvikon 810-Spectrophotometer (Bio-Tek Kontron Instruments, Neufahrn, Germany). The solution was kept in a quartz cuvette with a path length, d, of 1 cm. Extinction coefficients, ε(λ), were calculated using Lambert-Beer's Law (**S5**). Emission spectra of 1 µM Mant-GDP in buffer E supplemented with 5 mM $MgCl_2$ were recorded between 370 and 650 nm in steps of 2 nm (excitation around 355 nm) using a Spectrofluorometer FP 6500 (Jasco,

Grosse-Umstadt, Germany). The solution was kept in a quartz cuvette and stirred constantly to compensate for photo-bleaching. Spectra were reference-corrected (Fig. S6).

The denominator of Eq. S2 is used for normalization. The numerator was calculated by stepwise (2-nm) multiplication of the respective parameters and subsequent integration between 370 and 650 nm. Values exceeding the boundaries of the integration were negligible.

Finally, J was determined to be:

$$J(\lambda) = \frac{\int_{370}^{650} F_D(\lambda) \cdot \varepsilon_A(\lambda) \cdot \lambda^4 d\lambda}{\int_{370}^{650} F_D(\lambda) d\lambda} = \frac{1.9702 \cdot 10^{19}}{2.4645 \cdot 10^4} \approx 7.9945 \cdot 10^{14} \quad \left[M^{-1}\, cm^{-1}\, nm^4\right]$$

Determination of κ^2 and r_{calc} from MM and QM simulations

For the calculation of κ^2, it is important to consider that both fluorophores are attached to the nucleotide by very short linkers, and in case of the TNP moiety, the linker is even not freely rotatable. This makes it crucial to calculate the value of κ^2 directly from the structure of the simulated dimer and precludes using the value of 2/3 commonly used for a random distribution. In order to calculate κ^2, the transition dipole vector needs to be known. For this, we need to find the possible minimum structures of Mant-GDP and TNP-GDP. Therefore, the structures of Mant-ribose and TNP-ribose were quantum mechanically optimized in vacuum. First, quantum mechanical optimization runs were performed with random starting structures, which are gained by the shaking algorithm of Maximoby (18). Second, all rotatable groups have been scanned with a step size of 5° and all possible minima combinations have been used as starting structures for optimization. TNP-ribose results in only one structure with a reasonable energy whereas the Mant-ribose is more flexible, resulting in 10 possible minimum structures (Fig. S8). In addition, the Mant group can flip between the 2' and the 3' hydroxyl group of the ribose. Therefore, there are 20 possible structures for Mant-GDP and only one fixed structure for TNP-GDP (Fig. S9). In order to get a first impression if these vacuum structures would fit into the protein environment without steric clashes, the TNP-GDP was included on one site of the monomer and the different Mant-GDP structures (Fig. S8) on the other side of the dimer. The snapshot after 100 ns of the dimer simulation run was used as starting structure. During MM equilibration runs with fixed Mant and TNP we equilibrated the protein environment with the labeled substrate. Because all analyzed Mant and the TNP conformations point out of the binding niche they do not have clashes with the protein or are significantly influenced by the protein environment during our simulations. Thus, we assume that all Mant-GDP conformations obtained in vacuum are also possible in

the protein environment. This result is confirmed by the X-Ray structure of H-Ras with bound Mant-GPPNHP (1GNP) (22). In this structure there is no contact between the Mant-group and the Ras protein. In order to get an impression of the flexibility of the labeled structures we equilibrate the Mant-GDP and TNP-GDP structures in the protein environment. All 20 structures are stable during 5 ps QM/MM simulations. The Mant, the TNP and the ribose were treated quantum mechanically and the rest of the protein by molecular mechanics. All these tests are arguments for the reasonability of the vacuum structures. Only longer MM simulations including Mant and TNP would bring a clear proof of the flexibility. Therefore, validated MM parameters for Mant and TNP are needed, which is still a big challenge in computer science. Because there are no force-field parameters of Mant and TNP available, and we merely want to know the range of possible distances, we aligned the 20 structures of Mant-GDP and TNP-GDP combinations with the GDPs of the MM trajectories of the dimer runs. After an equilibration time of 50 ns, the distance between the middle of the aromatic ring of the Mant- and the TNP group was calculated for each 1-ns interval of the last 150-ns trajectories of the three independent runs. From this calculation, an overall averaged distance of r_{calc} = 46.1 ± 3.0 Å ($r_{calc,1}$ = 46.4 ± 3.0 Å; $r_{calc,2}$ = 45.8 ± 3.0 Å; $r_{calc,3}$ = 46.0 ± 2.9 Å) was predicted for the dimer (Fig. 4). The value κ^2 is required for the experimental estimation of the distance, r_{exp}, based on the FRET efficiency. By QM calculations of Mant and TNP in vacuum we obtain the transition dipole moment vector of each structure. With this we are able to calculate κ^2 by

$$\kappa^2 = \left(\cos\theta_T - 3\cos\theta_D \cos\theta_A\right)^2.$$

In which θ_A is the angle between the vector $\vec{r}_{calc}$ and the transition dipole moment of TNP, θ_D is the angle between $\vec{r}_{calc}$ and the transition dipole moment of Mant and θ_T is the angle between the transition dipole moment of Mant and TNP given by

$$\cos\theta_T = \sin\theta_D \sin\theta_A \cos\phi + \cos\theta_D \cos\theta_A .$$

Here ϕ is the azimuth between the planes given by the transition dipole moment of Mant and $\vec{r}_{calc}$ and by the transition dipole moment of TNP and $\vec{r}_{calc}$. A detailed Figure can be found in Höfling et al. (23) (Fig. 3). Following the same scheme by which the distance r_{calc} was determined, an overall averaged κ^2 of 0.41 ± 0.31 (κ_1^2 = 0.42 ± 0.33; κ_2^2 = 0.39 ± 0.30; κ_3^2 = 0.42 ± 0.33) was obtained from the simulations; this is slightly smaller than the commonly used value of 2/3 when an isotropic orientation is assumed. The very high value for the standard deviation of κ^2 reveals that we have almost an isotropic orientation. Due to sterical

restriction a small part of the configuration space is not populated and therefore the κ^2 is slightly smaller than 2/3.

Statistics in nucleotide exchange

For measuring τ_{DA}, Mant-GDP and TNP-GDP were added to the exchange buffer in equal concentrations (50 μM). In this case, the two different nucleotides are expected to bind Ras statistically, meaning that in case of a dimer-like formation of Ras, both heterogeneous pairs of nucleotides (MT) and homogenous pairs (MM and TT) will be bound within one dimer.

Consequently, the labeling of Ras dimers, assuming exactly equal affinities for GDP, Mant-GDP, and TNP-GDP, would result in four different dimers:

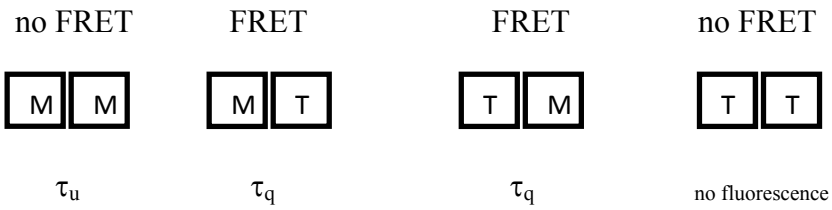

For the first dimer (MM), no FRET is possible and the fluorescence lifetime of Mant-GDP is τ_u (Fig. S6, right). Two of the shown dimers (MT, TM) will exhibit FRET and a lifetime τ_q. The last dimer (TT) carries two TNP-fluorophores which will not contribute to the detected signal since suitable band-pass-filters were used.

To extract τ_{DA} from the composed, measured signal, one has to investigate the distribution of the differently labeled GDPs on the Ras-molecules/dimers.

If

X_1 → number of unquenched Mant-GDP`s, revealing τ_u

X_2 → number of quenched Mant-GDP`s, revealing τ_q

Using Eq. S3

$$E = 1 - \frac{\tau_q}{\tau_u} \quad \Rightarrow \quad -\tau_q = (E-1)\cdot\tau_u \quad \Rightarrow \quad \tau_q = (1-E)\cdot\tau_u \qquad \textbf{(S3)}$$

a correlation between the measured and the theoretical Förster efficiency can be deduced as expressed by Eq. S4:

$$\mathrm{E}_{meas} = 1 - \frac{\tau_{DA}}{\tau_D} = 1 - \frac{x_1 \cdot \tau_u + x_2 \cdot \tau_q}{(x_1 + x_2) \cdot \tau_u} = 1 - \frac{x_1 \cdot \tau_u + x_2 \cdot (1 - E_{theo}) \cdot \tau_u}{(x_1 + x_2) \cdot \tau_u} \qquad \textbf{(S4)}$$

let be $x_1 + x_2 = x_3$,

$$\Rightarrow \; 1 - \frac{x_3 \cdot \tau_u - x_2 \cdot \mathrm{E}_{theo} \cdot \tau_u}{x_3 \cdot \tau_u} = 1 - \frac{\tau_u \cdot (x_3 - x_2 \cdot \mathrm{E}_{theo})}{x_3 \cdot \tau_u} = 1 - \frac{x_3 - x_2 \cdot \mathrm{E}_{theo}}{x_3}$$

$$= \frac{x_3 - x_3 + x_2 \cdot \mathrm{E}_{theo}}{x_3} = \frac{x_2}{x_1 + x_2} \cdot \mathrm{E}_{theo}$$

Since Ras binds Mant-GDP and TNP-GDP with different affinities (see below), x_1 and x_2 deviate from 2. By use of the determined probabilities (see below), the average amounts of homo- and hetero-dimers can be calculated as follows.

$$W(MM) = 0.61 \cdot 0.61 = 0.37 \quad \Rightarrow \quad 0.37 \cdot 4 = 1.48 \cdot MM$$
$$W(MT) = 0.61 \cdot 0.39 = 0.24 \quad \Rightarrow \quad 0.24 \cdot 4 = 0.96 \cdot MT$$
$$W(TM) = 0.39 \cdot 0.61 = 0.24 \quad \Rightarrow \quad 0.24 \cdot 4 = 0.96 \cdot TM$$
$$W(TT) = 0.39 \cdot 0.39 = 0.15 \quad \Rightarrow \quad 0.15 \cdot 4 = 0.60 \cdot TT$$

and thereby $x_1 = 2.96$, $x_2 = 1.92$.

This leads to a correction-factor of around 2.57. Thus, the measured FRET efficiency E_{meas} was multiplied by the correction-factor 2.57 to compensate for the statistics due to the flow-through-system.

Homo-FRET

When measuring τ_D, the fluorophore emission could possibly be decreased by homo-FRET. Experiments were performed to check for this, whereby either half or all of the GDP was exchanged for Mant-GDP. In the latter case, only homo-dimers are present. Corresponding lifetimes were compared to τ_D, but no decrease due to homo-FRET was observed. Additionally, there is no significant spectral overlap relevant to Mant-GDP (Fig. S6), indicating the absence of homo-FRET.

Determination of the nucleotide affinities to Ras

To check for differences in the nucleotide-affinities, we performed HPLC measurements of Ras that was previously exchanged with a mixture of Mant-GDP and TNP-GDP, as well as of the nucleotide mixture alone without protein. The nucleotide exchange was done as described above (see the section on quantum yield Q_0). HPLC measurements were performed using a reverse-phase column (ODS Hypersob 5 µm, 250 mm, 4.6 mm) on a Beckman System Gold Modules 125, 166 (Beckman Coulter, Krefeld, Germany) instrument with 50 mM KH_2PO_4/K_2HPO_4, 5 mM tetrabutyl ammonium bromide, 25% acetonitrile at pH 6.5. The areas under the related peaks (Mant-GDP and TNP-GDP) were integrated to obtain the overall absorbance (extinction) of the labeled nucleotides at 254 nm (Fig. S7). Based on the respective extinction-coefficients, the concentration of the treated nucleotides can be calculated by rearranging Lambert-Beer`s Law, Eq. S5:

$$E = \varepsilon \cdot c \cdot d \quad \Rightarrow \quad c = \frac{E}{\varepsilon \cdot d} \qquad \textbf{(S5)}$$

Here, c is the concentration of the nucleotide, E is the measured extinction at a given wavelength λ (here 254 nm), d is the path length of the transmitting light, and ε is the extinction coefficient of the nucleotide at λ.

The labeled nucleotides were received from Jena BioScience (Jena, Germany) and were delivered at pH 7.5. Exact concentrations of the delivered material were calculated using Eq. S5. For this, the respective extinctions were measured at 252 nm with a V-650 Spectrophotometer (Jasco, Grosse-Umstadt, Germany). For ε, the literature values (252 nm, pH 7.5) of Mant-GDP (22600 $M^{-1}cm^{-1}$) and TNP-GDP (24100 $M^{-1}cm^{-1}$) were used.

Subsequently, for a defined concentration of the labeled nucleotides (in buffer E, supplemented with 5 mM $MgCl_2$), the absorbance at 254 nm was measured with a V-650 (Jasco). The respective extinction coefficients (Mant-GDP and TNP-GDP at 254 nm, pH 6.5) were obtained by applying Eq. S5. These values of $\varepsilon_{\text{Mant-GDP, pH6.5}}$ (25400 $M^{-1}cm^{-1}$) and $\varepsilon_{\text{TNP-GDP, pH 6.5}}$ (26350 $M^{-1}cm^{-1}$) were used to determine the concentrations of Mant-GDP and TNP-GDP corresponding to the integrated areas (absorbance) obtained from HPLC measurements (Fig. S7). Comparing the relationship between these concentrations (Mant-GDP to TNP-GDP) in the solved and the Ras-bound cases delivers the ratio of the affinities of Ras for Mant-GDP and TNP-GDP. For the sake of simplicity, the following values were rounded.

The calculated ratio of 1.57 Mant-GDP : 1 TNP-GDP leads to different probabilities, W, for Mant-GDP and TNP-GDP to be bound by Ras, as follows.

W(Mant) = 1.57 : 2.57 = 0.61 W(TNP) = 1 : 2.57 = 0.39

Error Propagation for Calculation of Förster Radius R_0

R_0 depends on a variety of parameters. In general, in a function of variables $y = y(x_1, x_2, \ldots, x_n)$ with inherent uncertainties Δx_i, the overall uncertainty is given by Eq. S6

$$\Delta y = \left(\sum_{i=1}^{n} \left(\frac{\partial y}{\partial x_i} \cdot \Delta x_i \right)^2 \right)^{\frac{1}{2}} . \qquad \textbf{(S6)}$$

In the present situation, the function is the distance between the donor and acceptor $r = r(R_0, E)$, which was calculated by Eq. S7:

$$r = \left(\frac{R_0^6 \cdot (1-E)}{E} \right)^{\frac{1}{6}} \qquad \textbf{(S7)}$$

Including the Förster Radius $R_0 = 0.211 \cdot (\kappa^2 \cdot n^{-4} \cdot Q_0 \cdot J)^{1/6}$ and the FRET-Efficiency $E = (E_1+E_2)/2$ with $E_i = 1 - \tau_{DA(i)}/\tau_{D(i)}$, using values of $\kappa^2 = 0.41 \pm 0.31$, $n = 1.4 \pm 0.05$, $Q_0 = 0.53 \pm 0.05$, $J = 7.99 \cdot 10^{14} \pm 8 \cdot 10^{13}$, $\tau_{DA(1)} = 4.83 \pm 0.033$, $\tau_{D(1)} = 5.48 \pm 0.039$,

$\tau_{DA(2)} = 4.57 \pm 0.031$, $\tau_{D(2)} = 5.1 \pm 0.043$, this yields a distance of 46.4 ± 6.1 Å between donor and acceptor. The high overall uncertainty is due to the moderate accuracy of κ^2. Note that the use of $\kappa^2 = 2/3$ would lead to a distance of 50.3 Å which is within the error margin.

Expected FRET efficiency for randomly distributed Ras

Wolber and Hudson deduced an equation to calculate concentration-dependent FRET efficiencies for randomly distributed donors and acceptors on a two-dimensional surface (24). This takes into account that the fluorophores are attached to proteins with finite dimensions, and is given by Eq. S8:

$$E_{stat} = 1 - \left(A_1 \cdot e^{-k_1 c_A} + A_2 \cdot e^{-k_2 c_A} \right) \quad \textbf{(S8)}$$

Here, A_i and k_i are fitting parameters depending on the system and $c_A = (R_0)^2 \cdot C$ is the reduced acceptor surface density with C being the acceptor surface density. The parameters depend on the distance of the closest potential approach (R_c) of the donors and acceptors. This takes into account the fact that donors and acceptors are attached to proteins of finite size. A typical value of R_c for energy transfer in the case of protein-protein interactions can be approximated by the protein diameter. Similar approaches have been used regularly in literature (25).

According to Wolber and Hudson (24), the following parameters are best suited to approximate E_{stat} properly.

$A_1 = 0.6414$, $k_1 = 1.7400$, $A_2 = 0.3586$, $k_2 = 0.1285$

These parameters arise from numerical fits performed by them and are valid only if R_c/R_0 is around 1.0 and the concentration of fluorophores per Förster radius is within 0 and 0.6.

Since R_C was set to 4 nm, which is the diameter of Ras derived from the X-ray structure 1QRA, and R_0 was calculated to be 3.98 nm, R_c/R_0 indeed is almost exactly 1.0. For FRET measurements the surface concentration of Ras was adjusted to be in the range of 1.5 pmol per cm^2. The surface concentration of Ras was calculated using the area of the amide II band together with the absorption coefficient described in (26). A short calculation yields:

$c_A = R_0^2 \cdot C = R_0^2 \cdot 1.5 \cdot 10^{-12}$ mol/cm^2 Ras $\approx 14.31 \cdot 10^{-2}$ Ras per R_0^2

when applying R_0 = 39.8Å. Because of different affinities of Ras for Mant-GDP and TNP-GDP (1.57 : 1) → $c_A \approx 0.056$.

Therefore, Eq. S8 can be used here. Applying the appropriate parameters results in a FRET efficiency E_{stat} *of* 6.2%.

No Ras dimer in solution

The fluorescent nucleotides Mant-GDP and TNP-GDP were bound to Ras via the EDTA method (20), followed by a 1-min gel filtration step (Zeba Spin Desalting Columns, Pierce Biotechnology), in which the buffer was exchanged to buffer E supplemented with 5 mM $MgCl_2$. Three different TCSPC experiments were performed using the same devices and software as described above. In all three measurements, labeled Ras (solved in Buffer E + $MgCl_2$) was stirred within a quartz cuvette. Histograms were accumulated for the cases of (1.)

only Mant-GDP, (2.) Mant-GDP and GDP, or (3.) Mant-GDP and TNP-GDP bound to Ras. Lifetimes were calculated as described above and a FRET-efficiency of 3–4% was found.

Supporting References

1. Hess, B., C. Kutzner, D. van der Spoel, and E. Lindahl. 2008. GROMACS 4: Algorithms for Highly Efficient, Load-Balanced, and Scalable Molecular Simulation. Journal of Chemical Theory and Computation. 4: 435–447.

2. Van Der Spoel, D., E. Lindahl, B. Hess, G. Groenhof, A.E. Mark, et al. 2005. GROMACS: fast, flexible, and free. J Comput Chem. 26: 1701–1718.

3. Jorgensen, W.L., D.S. Maxwell, and J. Tirado-Rives. 1996. Development and Testing of the OPLS All-Atom Force Field on Conformational Energetics and Properties of Organic Liquids. Journal of the American Chemical Society. 118: 11225–11236.

4. Jorgensen, W.L., and J.D. Madura. 1985. Temperature and size dependence for Monte Carlo simulations of TIP4P water. Molecular Physics. 56: 1381–1392.

5. Ulmschneider, J.P., and M.B. Ulmschneider. 2009. United Atom Lipid Parameters for Combination with the Optimized Potentials for Liquid Simulations All-Atom Force Field. Journal of Chemical Theory and Computation. 5: 1803–1813.

6. Darden, T., D. York, and L. Pedersen. 1993. Particle mesh Ewald: An N·log(N) method for Ewald sums in large systems. The Journal of Chemical Physics. 98: 10089.

7. Berendsen, H.J.C., J.P.M. Postma, W.F. van Gunsteren, A. DiNola, and J.R. Haak. 1984. Molecular dynamics with coupling to an external bath. The Journal of Chemical Physics. 81: 3684.

8. Hess, B., H. Bekker, H.J.C. Berendsen, and J.G.E.M. Fraaije. 1997. LINCS: A linear constraint solver for molecular simulations. Journal of Computational Chemistry. 18: 1463–1472.

9. Frisch, M.J., G.W. Trucks, H.B. Schlegel, G.E. Scuseria, M.A. Robb, et al. 2003. Gaussian 03. Pittsburgh PA: Gaussian Inc.

10. Groenhof, G., M. Bouxin-Cademartory, B. Hess, S.P. De Visser, H.J.C. Berendsen, et al. 2004. Photoactivation of the photoactive yellow protein: why photon absorption triggers a trans-to-cis Isomerization of the chromophore in the protein. J. Am. Chem. Soc. 126: 4228–4233.

11. Warshel, A., and M. Levitt. 1976. Theoretical studies of enzymic reactions: dielectric, electrostatic and steric stabilization of the carbonium ion in the reaction of lysozyme. J. Mol. Biol. 103: 227–249.

12. Becke, A.D. 1993. Density-functional thermochemistry. III. The role of exact exchange. The Journal of Chemical Physics. 98: 5648.

13. Lee, Yang, and Parr. 1988. Development of the Colle-Salvetti correlation-energy formula into a functional of the electron density. Phys. Rev., B Condens. Matter. 37: 785–789.

14. Canutescu, A.A., A.A. Shelenkov, and R.L. Dunbrack Jr. 2003. A graph-theory algorithm for rapid protein side-chain prediction. Protein Sci. 12: 2001–2014.

15. Kouranov, A., L. Xie, J. de la Cruz, L. Chen, J. Westbrook, et al. 2006. The RCSB PDB information portal for structural genomics. Nucleic Acids Res. 34: D302–305.

16. Güldenhaupt, J., Y. Adigüzel, J. Kuhlmann, H. Waldmann, C. Kötting, et al. 2008. Secondary structure of lipidated Ras bound to a lipid bilayer. FEBS J. 275: 5910–5918.

17. Reuther, G., K.-T. Tan, J. Köhler, C. Nowak, A. Pampel, et al. 2006. Structural model of the membrane-bound C terminus of lipid-modified human N-ras protein. Angew Chem Int Ed Engl. 45: 5387–5390.

18. Höweler, U. 2007. MAXIMOBY. Altenberge, Germany: CHEOPS.

19. Hiratsuka, T. 1983. New ribose-modified fluorescent analogs of adenine and guanine nucleotides available as substrates for various enzymes. Biochim. Biophys. Acta. 742: 496–508.

20. Lenzen, C., R.H. Cool, H. Prinz, J. Kuhlmann, and A. Wittinghofer. 1998. Kinetic analysis by fluorescence of the interaction between Ras and the catalytic domain of the guanine nucleotide exchange factor Cdc25Mm. Biochemistry. 37: 7420–7430.

21. Stieglitz, B., C. Bee, D. Schwarz, O. Yildiz, A. Moshnikova, et al. 2008. Novel type of Ras effector interaction established between tumour suppressor NORE1A and Ras switch II. EMBO J. 27: 1995–2005.

22. Scheidig, A.J., S.M. Franken, J.E. Corrie, G.P. Reid, A. Wittinghofer, et al. 1995. X-ray crystal structure analysis of the catalytic domain of the oncogene product p21H-ras complexed with caged GTP and mant dGppNHp. J. Mol. Biol. 253: 132–150.

23. Hoefling, M., N. Lima, D. Haenni, C.A.M. Seidel, B. Schuler, et al. 2011. Structural heterogeneity and quantitative FRET efficiency distributions of polyprolines through a hybrid atomistic simulation and Monte Carlo approach. PLoS ONE. 6: e19791.

24. Wolber, P.K., and B.S. Hudson. 1979. An analytic solution to the Förster energy transfer problem in two dimensions. Biophysical Journal. 28: 197–210.

25. Dewey, T.G., and M.M. Datta. 1989. Determination of the fractal dimension of membrane protein aggregates using fluorescence energy transfer. Biophys. J. 56: 415–420.

26. Kötting, C., J. Güldenhaupt, and K. Gerwert. 2012. Time-resolved FTIR spectroscopy for monitoring protein dynamics exemplified by functional studies of Ras protein bound to a lipid bilayer. Chemical Physics. 396: 72–83.

Supporting Figures

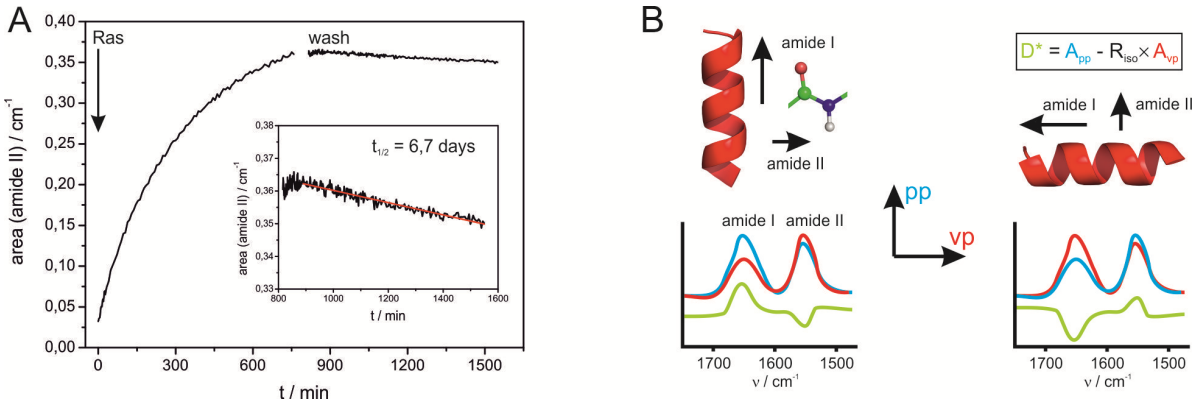

Fig. S1: (A) Binding of lipidated Ras to a solid supported POPC bilayer. (B) Calculating the dichroitic difference spectra D* allows for the determination of the orientation of the absorbing groups e.g. α-helices. The scaling factor R_{iso} was calculated using wavenumber-dependent refractive indices of germanium and H_2O. n(Ras) was taken as 1.45.

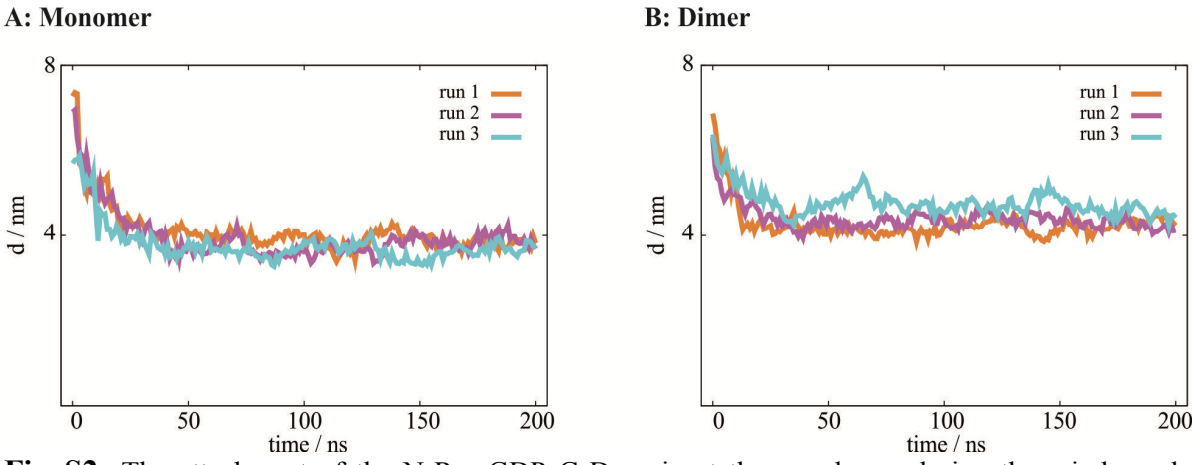

Fig. S2: The attachment of the N-Ras·GDP G-Domain at the membrane during three independent 200-ns MD simulations of a Ras monomer (A) and a Ras dimer (B) are depicted. The graphs show the distance d between the center of mass of the protein and the membrane (see Fig. 2) during the simulation time. After 50 ns the protein is stably attached at the membrane.

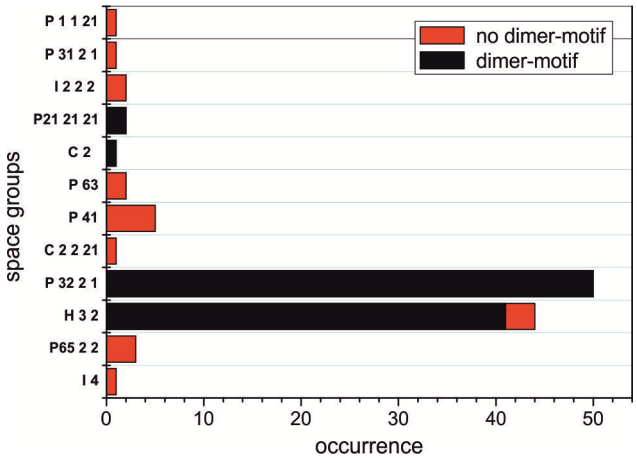

Fig. S3: Analysis of the available X-ray structures of Ras. Fifty of the 71 structures show the dimer.

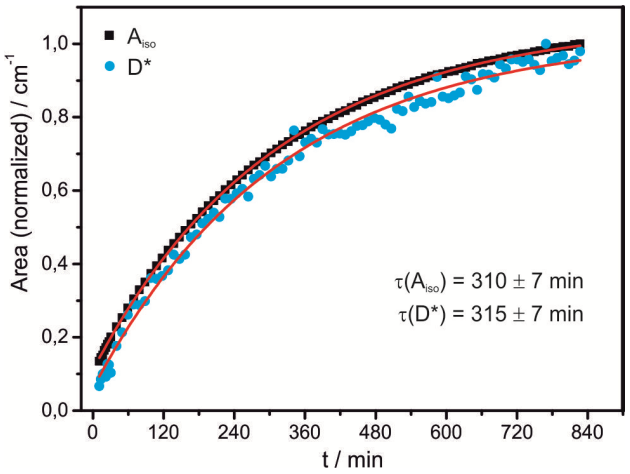

Fig. S4: Normalized kinetics of the amide II band area and the area of D* in the amide I region of Ras during immobilization to the membrane evolve with similar time constants. This shows that the D* signal is independent of surface coverage, eliminating crowing as a driving force.

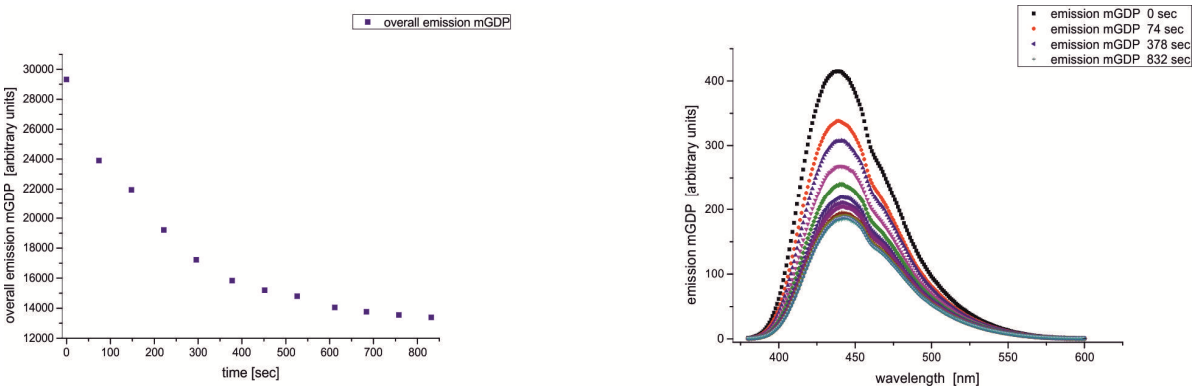

Fig. S5: Time-course of overall Mant-GDP-emission (left), Measurement series of Mant-GDP-emission-spectra (right).

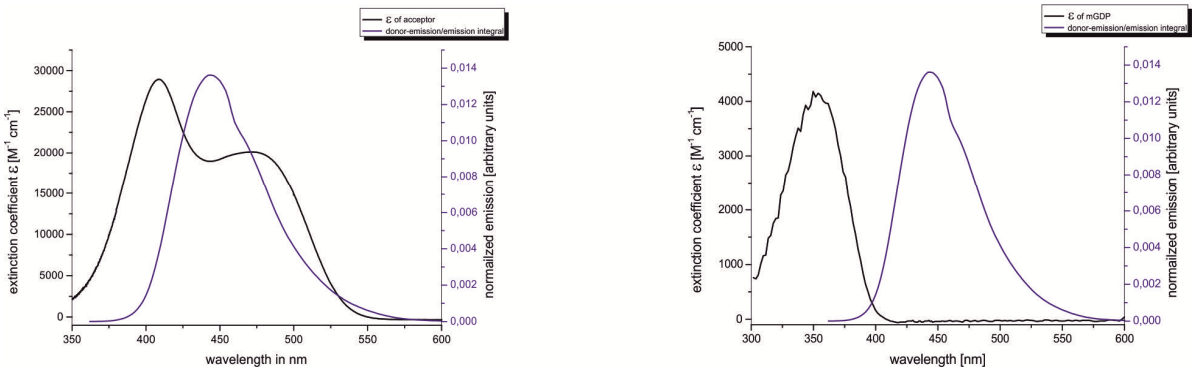

Fig. S6: Relationship between the wavelength-dependent molar extinction coefficient ε(λ) of a FRET-acceptor and the emission-spectrum of a corresponding FRET-donor. TNP-GDP is the acceptor and Mant-GDP donor (left); Mant-GDP is both the acceptor and the donor (right).

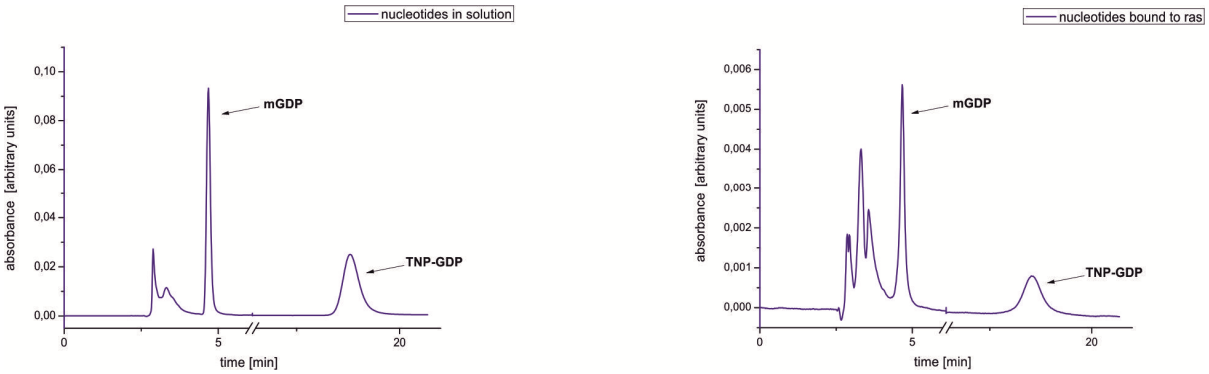

Fig. S7: Absorbance spectra recorded at 254 nm via HPLC; labeled GDP (50 mM MES, 100 mM NaCl, 5 mM $MgCl_2$, 1 mM TCEP, pH 6.5) in solution (left) and bound to Ras after nucleotide exchange (right).

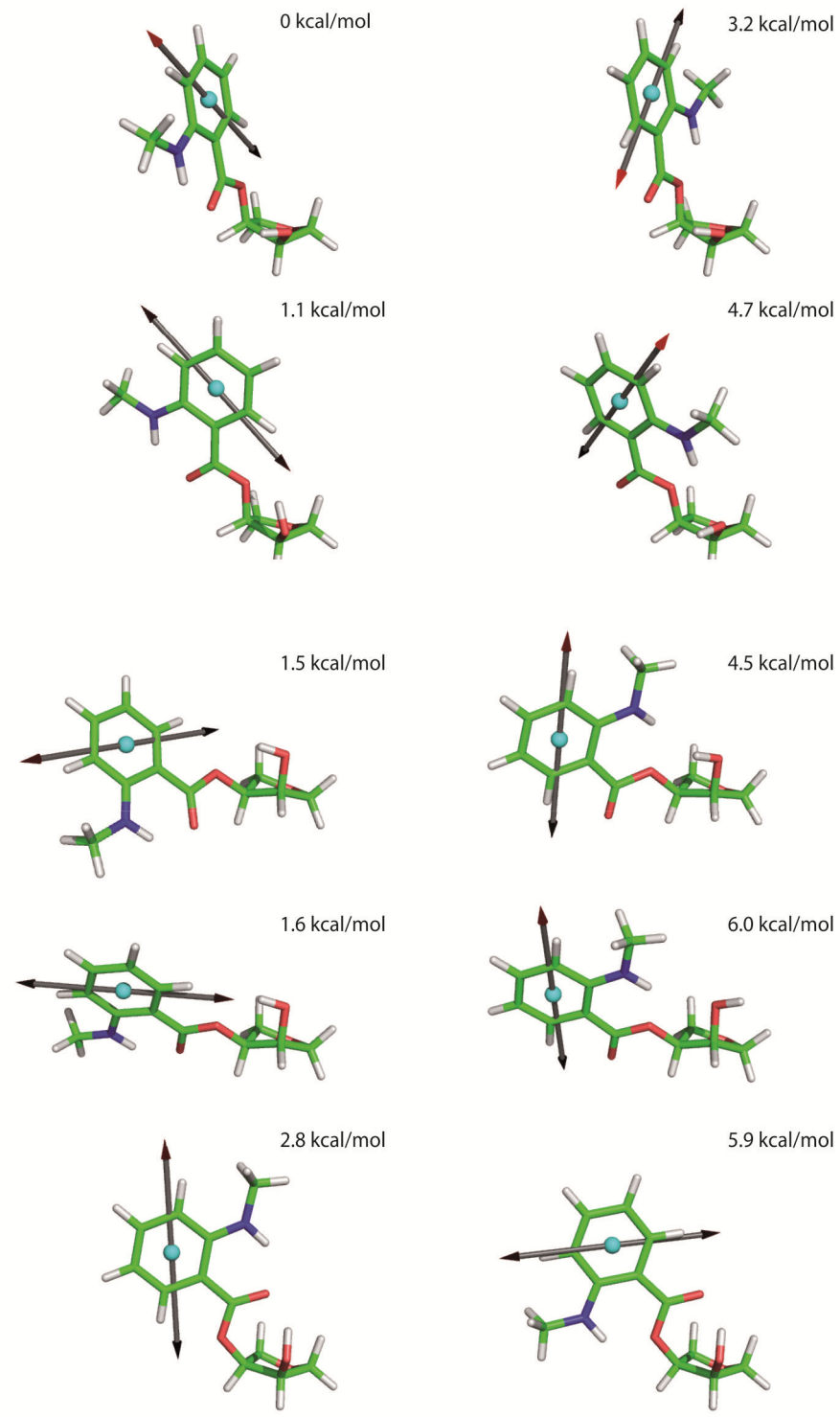

Fig. S8: Minimum conformations of Mant ribose in vacuum with their transition dipole moments. Shown are the 10 structures with the lowest conformational energies reached by quantum mechanical optimization with the B3LYP/6-31G* level of theory. The given conformational energy value in each case is the energy difference relative to the lowest observed conformational energy.

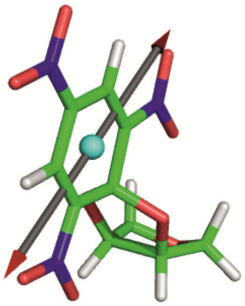

Fig S9: Minimum conformation of TNP ribose in vacuum with its transition dipole moment. Shown is the structure with the lowest conformational energy reached by quantum mechanical optimization with the B3LYP/6-31G* level of theory.

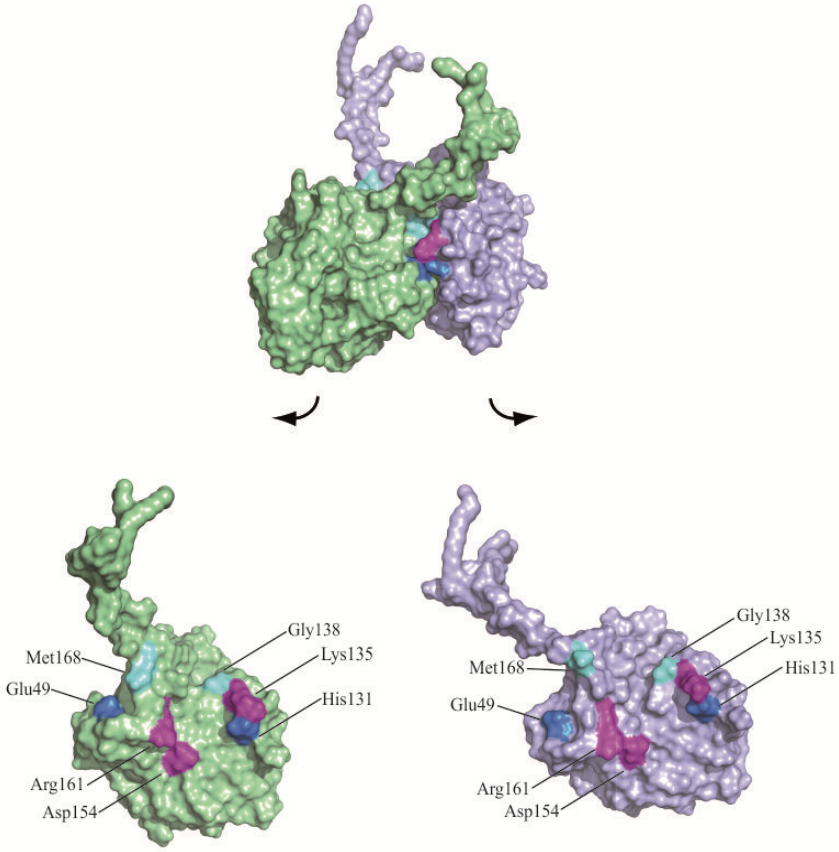

Fig S10: Surface representation of the dimer interface. From our MM simulations, we identified the highlighted amino acids participating in the intermolecular stabilization of the dimer. Magenta means interaction by hydrogen bonds, cyan by van-der-Waals interactions, and blue by both.